

The Effect of Applying Magnetic Fields During Welding AISI-304 Stainless Steel on Stress Corrosion Cracking

F.F. Curiel¹, R. García¹, V.H. López^{1,*}, M.A. García², A. Contreras³, M.A. García⁴

¹ Instituto de Investigación en Metalurgia y Materiales, Universidad Michoacana de San Nicolás de Hidalgo, Edificio “U”, Ciudad Universitaria, Morelia, Mich., México, CP 58060.

² Faculty of Metallurgy, Autonomous University of Coahuila, Carretera 57, km 5, Monclova, Coahuila, México, CP 25720.

³ Instituto Mexicano del Petróleo, Eje Central Lázaro Cárdenas Norte 152, San Bartolo Atepehuacan, México, C.P. 07730.

⁴ Centro Universitario de Ciencias Exactas e Ingenierías, Universidad de Guadalajara. Depto. de Electrónica. 1421 Boulevard Marcelino García Barragán, Guadalajara, Jalisco, México, CP 44420.

*E-mail: vhlopez@umich.mx

Received: 20 October 2020 / Accepted: 24 December 2020 / Published: 31 January 2021

The stress corrosion cracking (SCC) behavior of AISI-304 stainless steel welded under the simultaneous application of electromagnetic fields of low intensity (0 to 28 mT) was studied. The plates were gas metal arc welded (GMAW) with an ER309L filler wire. The susceptibility to SCC was investigated using slow strain rate tests (SSRT) performed at strain rate of $1 \times 10^{-6} \text{ s}^{-1}$ in a glass autoclave containing a magnesium chloride solution (20%-MgCl₂) at room temperature and 80 °C. Observation in the scanning electron microscope (SEM) showed that most of the specimens failed in the weld bead, exhibiting a ductile fracture with intergranular cracking. The SCC mechanism for welds of 304 stainless steel might be due to the formation of martensite at the grain boundaries. It was found that the magnetic field can modify the microstructure in the welded joints at a micro-level. This effect results in an improvement on the susceptibility to SCC. Secondary cracks were seen in the SSRT specimens in the SEM, most of them originated by pits. These features were more evident for the as-received 304 base metal and the 22mT welded joint tested at 80 °C. The susceptibility to SCC increased at 80 °C as compared to ambient temperature. The welded joints that exhibited better resistance to cracking and pitting were specimens welded with magnetic fields of 9 and 28 mT.

Keywords: Stress Corrosion Cracking, Austenitic Stainless Steels, Welding, Magnetic Field.

1. INTRODUCTION

Austenitic stainless steels (ASSs) AISI 304 and 316 are extensively used in the petrochemical industry and in super heater tubes of power boilers due to their superior mechanical properties at elevated

temperatures. However, their relatively high carbon content makes them susceptible to sensitization and SCC [1-3]. The resistance to SCC of stainless steels is highly influenced by different factors such as chemical composition, microstructural characteristics, thermo-mechanical history and operating environment. For example, ferritic and martensitic stainless steels are susceptible to hydrogen embrittlement in chloride rich mediums [4].

The SCC term is usually employed to describe the premature failures that occur in components like pressurized water reactors in service, these fails occur by the generation of cracks and their propagation in acidic solutions [5]. The SCC in many components is the result of the interplay between applied stresses and electrochemical reactions due to corrosive environments. The onset of the SCC phenomena, mostly initiates at the metal surface [6] preferably in sites like precipitates, second phases, weld beads, inclusions or any site where pitting is favored and subsequently break down of the component may occur due to crack growth and its catastrophic propagation [7].

The main causes of SCC include; thermal history of the material (time, pressure and temperature of operation), sensitization induced normally during secondary processing and the environment where the components are exposed. ASSs were designed to resist corrosion in acidic solutions and terms such as chloride-SCC and polythionic acid-SCC are frequently used to describe the behavior of these alloys to SCC phenomena [8]. In relation to SCC, sensitization in stainless steels refers to the precipitation of chromium-rich carbides, depleting chromium areas close to grain boundaries and making them thereby susceptible to intergranular corrosion. This phenomenon is aggravated when stainless steel is subjected to a welding thermal cycle leading to weld decay in the heat-affected zone (HAZ). Thus, sensitization is directly related to SCC resistance and therefore reducing or eliminating the susceptibility of ASSs to localized corrosion will have a significant impact on the SCC susceptibility.

MgCl₂ is one of the most popular solutions used to evaluate the susceptibility to SCC behavior in ASSs [9]. Due to its aggressivity, MgCl₂ is often used in concentrate solutions in the laboratory and its application is standardized in ASTM-G36 [10]. Fusion welding processes like gas metal arc welding and gas tungsten arc welding are widely employed in the stainless steel industry to join the different types of stainless steels. Profound metallurgical transformations may occur in the HAZ as a consequence of the welding heat input [11] leading to susceptibility to intergranular corrosion (IGC) and transgranular corrosion (TGC) [12, 13]. Sensitization, IGC and TGC may be enhanced by introducing cold working prior to welding [14, 15].

The application of external magnetic fields during welding has proved that the susceptibility to IGC can be overcome in ASSs [16-18]. Chromium depletion in the grain boundaries and sensitized zones in the HAZ can be retarded and healed, respectively, due to the presence of an external magnetic field during welding, improving the corrosion resistance [16, 17]. Recently, this technique has been used in duplex stainless steels seeking to avoid microstructural changes and enhancing the corrosion resistance in GMA welds [19, 20]. In addition, experimental results suggest that for certain magnetic fields intensities and orientations the corrosion resistance can be improved in the HAZ [21].

Curiel et. al. [22] suggested that the interaction between the magnetic field generated by the electric arc and the external magnetic field can produce the vibration of chromium atoms, which as a consequence can delay diffusion at preferential sites. Thus, the depletion of chromium in grain boundaries and in the surroundings of second phases may be reduced. Besides, twins, dislocations

density and α -martensite formed during cold working enable a faster path for chromium diffusion. Furthermore, magnetostriction in ferrite and martensite may also contribute to redistribute and homogenize alloying elements in the HAZ of AISI 304 stainless steel [16].

External magnetic fields, in the order of tens of mT, have been used during fusion welding of stainless steels seeking to modify the grain structure of the weld metal [23, 24]. High magnetic fields have been employed to modify solid phase transformations [25, 26]. In this work, the effect of varying the magnetic field applied during welding AISI 304 stainless steel on the SCC susceptibility was studied through SSR tests in a magnesium chloride solution (20%-MgCl₂) at room temperature and 80° C. If previous findings showed improvement in the degree of sensitization in the HAZ when applying external magnetic fields during welding, then this practice is also very likely to have a positive impact on SCC behavior of AISI 304 welded joints.

2. EXPERIMENTAL PROCEDURE

2.1 Materials and welding parameters

Table 1. Chemical composition of the AISI 304 ASS plates and electrode employed (wt.%).

Material	C	Mn	Cr	Ni	Si	P	S
AISI 304	0.058	1.512	18.56	8.08	0.352	0.024	0.008
ER309L	0.04	1.90	22.0	12.0	1.0	0.025	0.0008

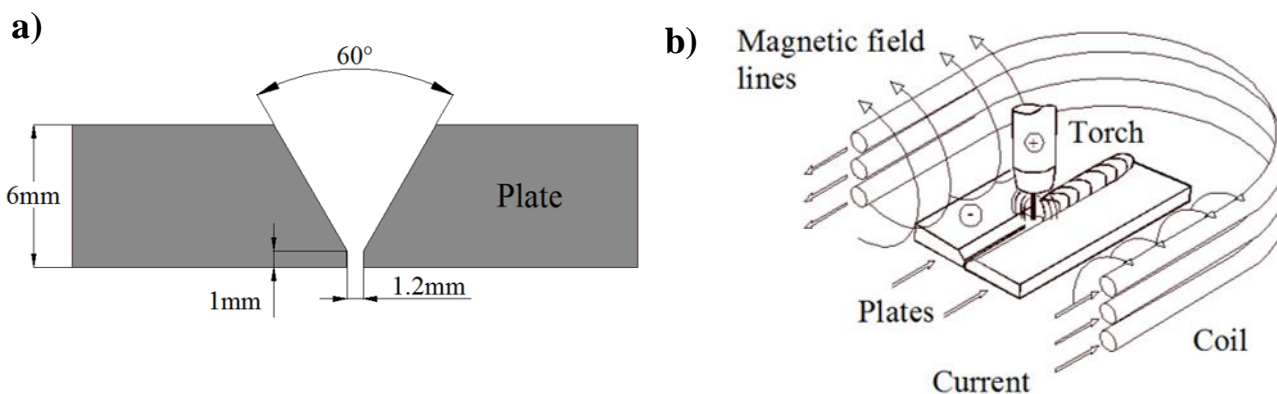


Figure 1. a) Schematic of the single V-groove joint used to weld the plates and b) experimental setup to induce an external magnetic field during welding.

Plates of commercial ASS AISI-304 with 6 mm in thickness were used. The chemical composition of the plates and filler wire (ER309L, 1.2 mm in diameter) are shown in Table 1. In order to perform the welding process, the plates were machined according to the configuration shown in Figure 1a). The plates were welded by using the GMAW process with direct current electrode positive: at 27 V, 190 A and shielding the weld pool with 98% Ar +2% O₂ flowing at 30 L/min. The ER309L electrode

was fed into the V-groove at 180 mm/s with a stick out of 10 mm while the welding torch was displaced at 3.6 mm/s. During welding an axial magnetic field was applied with intensities of 0, 9, 12, 22 and 28 mT. The direction of the magnetic field lines was parallel to the electrode as illustrated in Figure 1b).

2.2 Slow strain rate tests (SSRT)

The specimens used for SSR tests were obtained from commercial AISI 304 ASS (yield strength: 345 MPa and ultimate tensile strength: 670 MPa). After welding, cylindrical tensile specimens with 25.4 mm (1 in) and 3.81 mm (0.150 in) in gauge length and diameter, respectively, (with the weld bead in the center) were obtained as shown in Figure 2. Specimens were carefully fabricated according to the NACE-TM0198 standard [27].

The SSR technique is accepted and applied worldwide, using strain rates in the order of $1 \times 10^{-6} \text{ s}^{-1}$. Successful results have been obtained in materials such as carbon and stainless steels and different alloys. Thus, the application of the SSRT is sought after because an assessment of the susceptibility to SCC in corrosive environments can be determined in a reasonable period of time for a given material [28].

The SSR tests were carried out by placing the specimens in a glass autoclave filled with an aqueous 20 wt.%-MgCl₂ solution as shown in Figure 3a) and heating the system to 80 °C by means of an electrical resistance surrounding the container. The tests were performed with an Inter-Corr machine type MCERT (Mobile Constant Extension Rate Tests) with a load capacity of 44 kN and a total extension of 50 mm. The glass autoclave was placed and fixed in the MCERT machine as shown in Figure 3b).

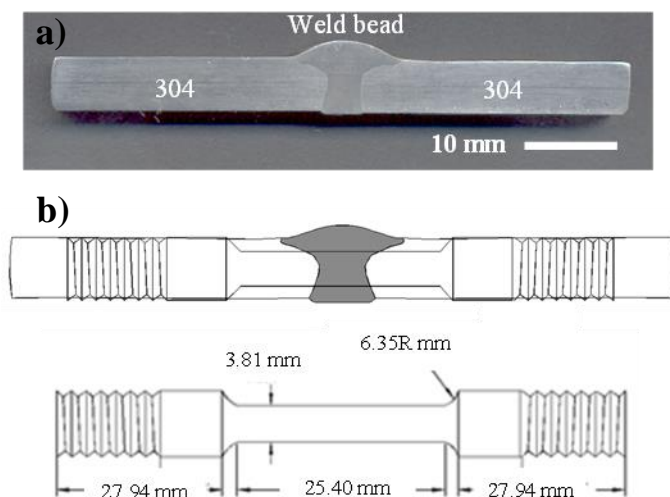


Figure 2. a) Transverse view of the welded joint and b) specimen geometry with dimensions (mm) for SSRT.

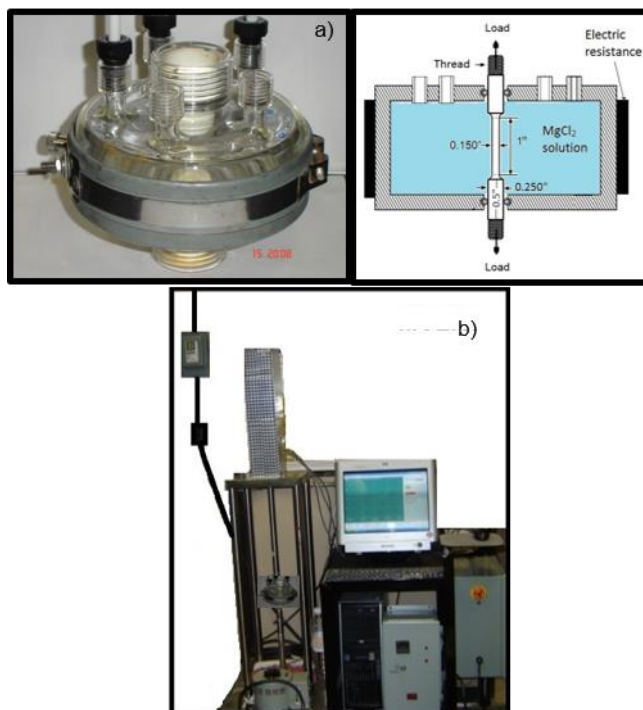


Figure 3. a) Glass autoclave and b) MCERT machine used for the SSR tests.

First of all, a test of the as-received base metal was performed in air, as an inert atmosphere, at room temperature (20 °C) for reference. Then, the tests were carried out by immersing the specimens in the magnesium chloride solution with a pH value of 6; as-received base metal, welds without magnetic field and with the application of different magnetic fields were tested. The essays were performed at room temperature (20°C) and 80°C applying a strain rate of $1 \times 10^{-6} \text{ s}^{-1}$. Finally, the fractured specimens obtained from the SSR tests were analyzed in detail in the SEM.

2.3 Assessment of the susceptibility to SCC

The susceptibility to SCC was evaluated according to NACE TM-0198 and ASTM G-129 standards for SSR tests [27, 29]. The mechanical properties obtained from these tests were used in the SCC assessment by calculating the corresponding indexes. A SCC index greater than 0.8 means high resistance to environment assisted cracking whereas lower values indicate that the material is susceptible to SCC. Thus, to maximize the SCC resistance, it is desirable to obtain index values close to unit.

Nonetheless, when the SCC index is less than 0.8, metallographic observation should be performed to determine whether or not there is susceptibility to SCC. When it is uncertain to establish the susceptibility to SCC by evaluating the mechanical properties, it is necessary to examine the cracks in the longitudinal section to differentiate cases of corrosion instead of SCC, because the cracks may initiate from pits [30-32].

After performing the SSR tests, the fracture surfaces were observed in an environmental scanning electron microscope (ESEM) Philips XL-30. The susceptibility to SCC was expressed in terms of the

percentage of reduction in area (%RA) as calculated by the following expression according to the NACE TM-0198 standard [27]:

$$\%RA = \frac{(D_i^2 - D_f^2)}{D_i^2} \times 100 \quad (1)$$

where D_i and D_f are the initial diameter of the gauge section of the specimen and the final diameter of the fracture surface of the tensile specimen, respectively.

The ratio in the reduction of area (RRA) after fracture for the specimen in the test environment (RA_{sol}) to the corresponding value determined in the controlled environment (RA_{air}) was calculated according to the following expression:

$$RRA = \frac{RA_{sol}}{RA_{air}} \quad (2)$$

Additionally, the time to failure ratio (TFR) was evaluated in order to have another parameter to assess the SCC susceptibility.

$$TFR = \frac{TF_{sol}}{TF_{air}} \quad (3)$$

Where TF_{sol} is the time to failure determined for the material in the test environment and TF_{air} is the time to failure as determined from the reference test in environmental air.

The plastic elongation ratio (PER) was calculated according to the following equations:

$$\%PE = \left[\frac{E_F}{L_I} - \left(\frac{\sigma_F}{\sigma_{PL}} \right) \left(\frac{E_{PL}}{L_I} \right) \right] \times 100 \quad (4)$$

$$PER = \frac{PE_{sol}}{PE_{air}} \quad (5)$$

Where PE is the plastic strain to failure (%), E_F is the elongation at failure, E_{PL} is the elongation at proportional limit, L_I is the initial gauge length, σ_F is the stress at failure and σ_{PL} is the stress at proportional limit.

3. RESULTS AND DISCUSSION

3.1 Macro and microstructural characteristics of the welded joints

Plates of AISI 304 ASS were GMA welded with the simultaneous application of an axial magnetic field with intensities of 0, 9, 12, 22 and 28 mT. Figure 4 shows the transverse views of the welded joints with the different magnetic fields applied. It can be seen that the width of the weld bead is narrower as the intensity of the magnetic field increases whereas the height of the weld reinforcement gradually increases. At magnetic fields greater than 22 mT, the quality of the weld was affected, showing lack of fusion in the root and the presence of excessive spattering on the surface of the plates of the welded joints. From these welded plates, SSRT specimens were cut and machined in order to evaluate the SCC resistance in the $MgCl_2$ solution.

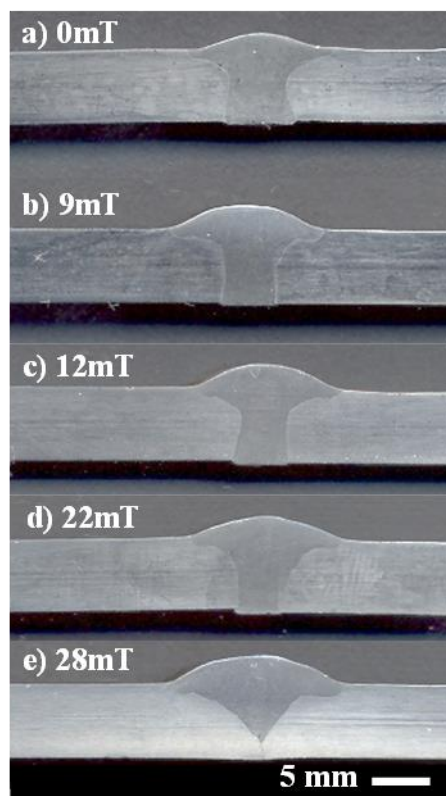


Figure 4. Macrographs of cross sections of the welds.

Figure 5 shows the characteristic microstructure of the base metal in the as-received condition and the microstructure in the HAZ after welding with different magnetic field intensities. The microstructure of the base metal is constituted by an austenitic matrix with traces of ferrite (dark lines) aligned in the rolling direction of the plates and α' -martensite laths which were induced during cold working in the manufacturing process of the plates. The presence of δ -ferrite in ASS generally improves resistance to CI-SCC, because it acts as interference with the crack propagation in the austenitic matrix, therefore, considerable quantities of ferrite must be present in ASS in order to improve the ductility. In addition, a fraction up to 5% of δ -ferrite is desirable in ASSs in order to prevent hot cracking during welding. The optical micrographs taken at the HAZ of the welded joints show some changes regarding the features appreciated in the as-received 304 ASS. The 9 mT sample exhibits thin and coarse needles of α' -martensite along with δ -ferrite. The other samples show a slight reduction in the content of α' -martensite, appearing mostly as coarse needles, and the presence of δ -ferrite prevails. From these micrographs, it is not possible to categorically ascertain if there is a significant variation in the content of δ -ferrite.

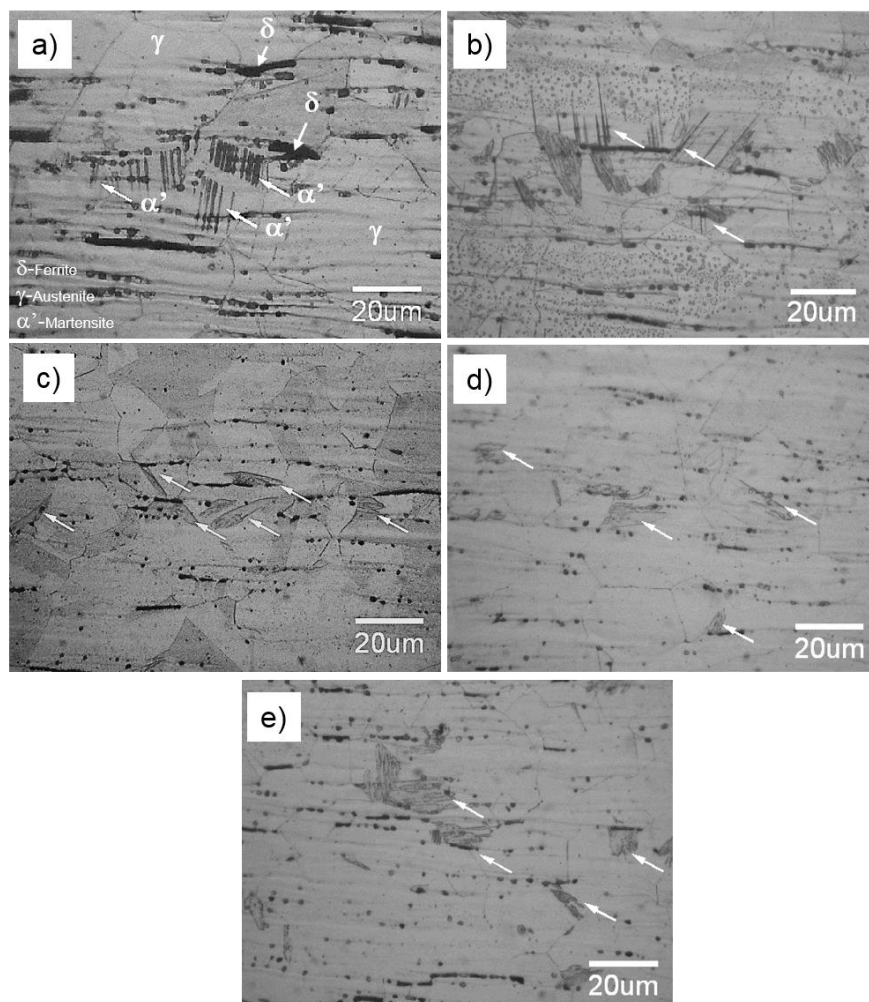


Figure 5. Microstructure of AISI 304 ASS; a) as-received, and in the HAZ after welding with magnetic fields of b) 9 mT, c) 12 mT, d) 22mT and e) 28 mT.

Electromagnetic stirring of the weld pool has been used during welding of stainless steels by applying an external magnetic field, this practice seeks to change the typical columnar grain growth of the weld metal during freezing [23, 24]. In the solid state, however, experimental findings suggest that the electromagnetic interaction of low intensity generated by the external magnetic field and the inherent magnetic field of the welding current enable Cr redistribution in the austenitic base metal during the welding thermal cycle reducing Cr depletion in the HAZ and decreasing in consequence the degree of sensitization [16, 17]. Zhengwu et al. [33] observed that the HAZ is reduced in tens of micrometers when a magnetic field between 18 to 24 mT was applied during hybrid welding of 316L. Similar results were previously reported by Garcia et al. [19] with a duplex stainless steel. Thus, a number of positive effects are well documented about fusion welding assisted by external magnetic fields.

Figure 6 shows the characteristic microstructures at the center of the weld metal as function of the magnetic field applied during welding. The fusion zone exhibits the typical AF solidification mode expected for an ER-309L filler. There are, however, notable differences in the weld metal between the microstructures of the samples. The micrograph of the 0 mT weld, Figure 6a), consists of a coarse austenitic dendritic matrix with equally coarse ferrite non-homogeneously distributed in the

interdendritic spaces. Interestingly, the 9 mT weld presents a refined equiaxed austenitic structure with an evident reduction of the interdendritic spaces where thin δ -ferrite is allocated and evenly distributed forming an almost continuous network. This effect is irrefutably ascribed to the electromagnetic stirring of the weld pool during welding and solidification. The optical images for the 12 and 22 mT welds, Figures 6c) and 6d), respectively, reveal that increasing the magnetic field applied during welding did not promote further grain refinement of the microstructure in the weld metal. Instead, for these samples a reduction in the volume fraction of interdendritic δ -ferrite seems to take place. Thus, as the electromagnetic field applied increases, δ -phase decreases and thereby the possibility of strain-induced martensite is greater if the welded joints are subjected to strain [34].

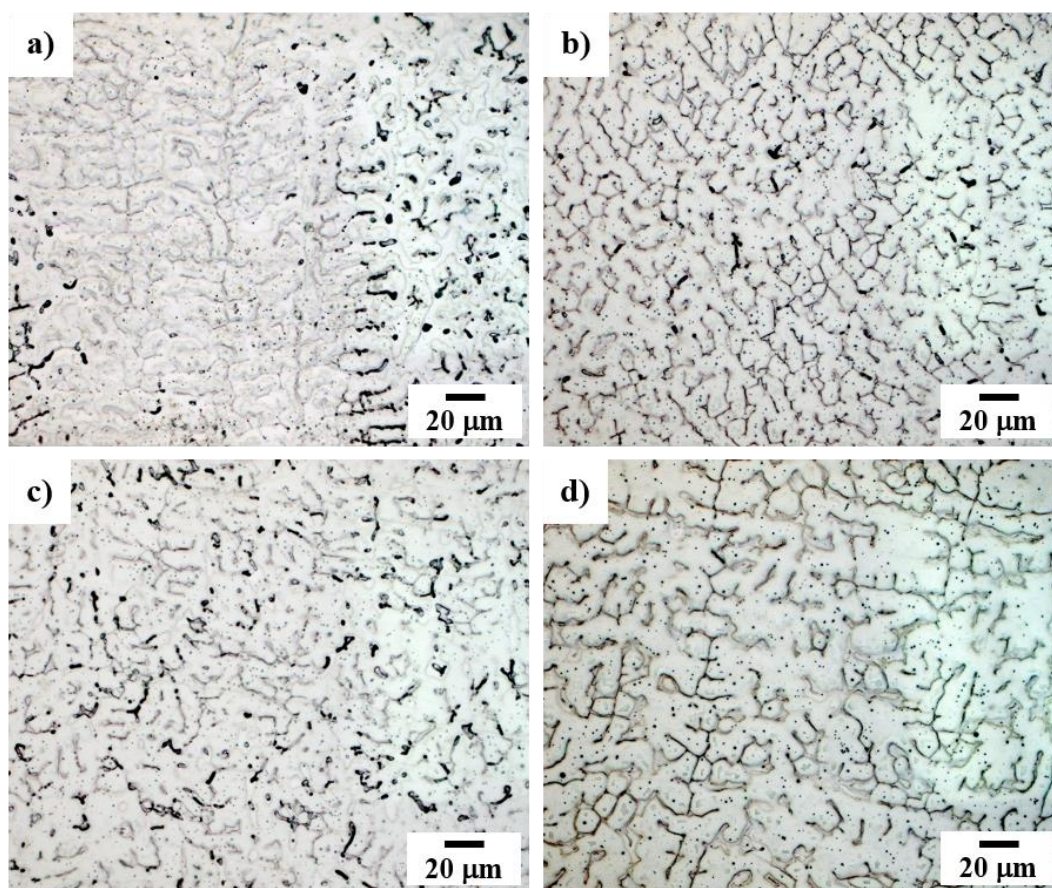


Figure 6. Microstructures at the center of the weld metal; a) 0, b) 9, c) 12 and d) 22 mT.

3.2 Behavior of the welds during SSR testing

Stress-strain profiles obtained from the SSR tests performed for the different welding conditions are shown in Figure 7a) and 7b) for specimens tested at 20 and 80 °C, respectively. In order to analyze these profiles, results of ultimate tensile strength (UTS), plastic elongation (PE), time to failure (TF), elongation (EL), strain (ϵ) and reduction area (RA) were obtained and the data is listed in Table 2. From these properties, ratios of RAR , PER , TFR , ELR , and ϵR , were calculated for both temperatures and the

results of the average SCC index (I_{sc}) are also given in the last column of Table 2. Bear in mind that a SCC index greater than 0.8 means that AISI 304 stainless steel is resistant to SCC. The samples found with an indication of SCC less than 0.8 were analyzed in the SEM to evaluate the presence of cracks.

The results of the SSRT revealed that samples welded with 12 and 22mT and tested at 20 and 80°C, respectively, show susceptibility to SCC in the test solution. Nevertheless, SEM observation must be performed in order to corroborate the presence of cracks in these specimens. It is noted that the strength, elongation and strain decreases slightly when the samples are exposed to the 20%-MgCl₂ solution at 80°C as compared with samples tested at room temperature (20°C).

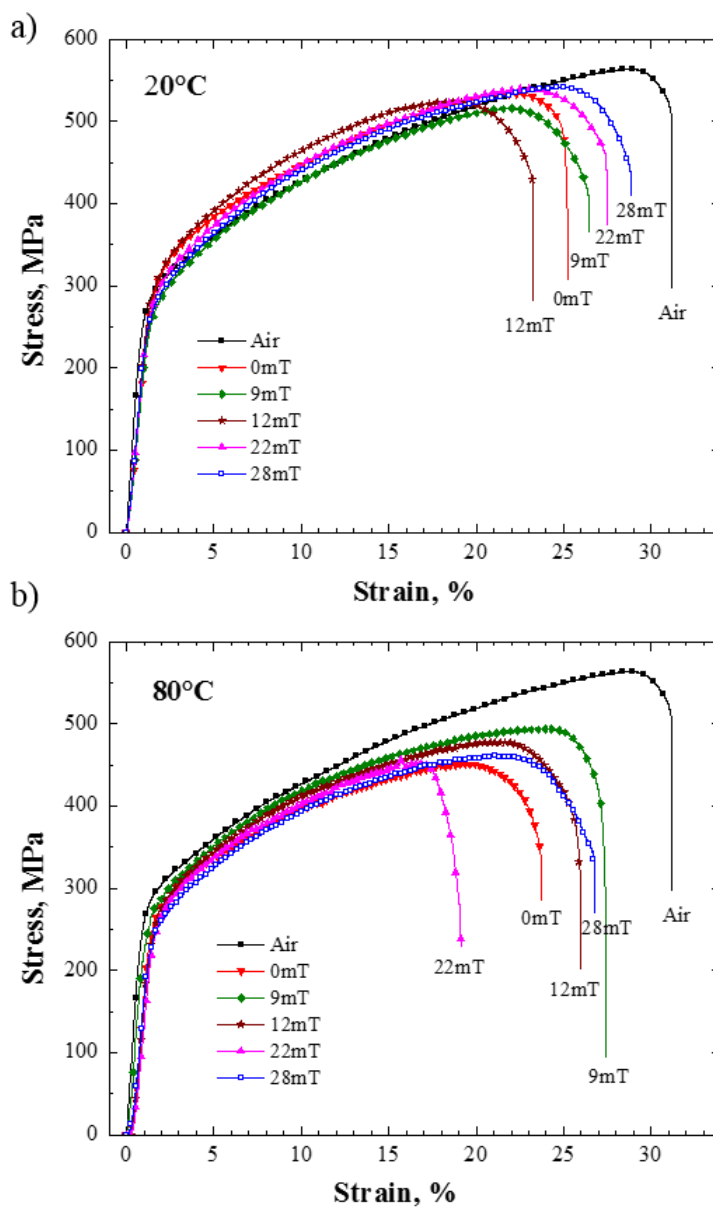


Figure 7. Typical stress versus strain profiles obtained from the SSRT.

In order to analyze the effect of the applied magnetic field during welding along with temperature on the SCC susceptibility, Figure 8 shows the average SCC index as function of the different ratios

obtained from mechanical properties of the SSRT. The susceptibility indexes of the specimens welded without the application of external magnetic field are in the limit value to exhibit SCC. In general, for both temperatures there is a trend to increase the SCC resistance as the magnetic field increases. Besides, it can be observed that SCC susceptibility increases with temperature, except for samples welded with 12 mT, where the SCC susceptibility is greater at 20°C than at 80°C.

Table 2. Mechanical properties and SCC index obtained from SSR tests at 20 and 80°C.

Condition	UTS [MPa]	PE [%]	TF [h]	EL [mm]	ϵ [%]	RA [%]	RAR	ϵR	ELR	TFR	PER	I_{scc}
Air	564	27.5	91.35	7.91	31.2	69	1	1	1	1	1	
0mT-20°C	534	22	73.6	6.4	25.1	58	0.85	0.8	0.81	0.8	0.8	0.81
0mT-80°C	451	20.6	69.29	6.02	23.6	62	0.91	0.76	0.85	0.76	0.74	0.80
9mT-20°C	515	23.2	77.4	6.72	26.4	69	1	0.85	0.84	0.85	0.85	0.88
9mT-80°C	493	24.3	81.55	6.96	27.1	55	0.8	0.87	0.96	0.89	0.89	0.88
12mT-20°C	524	20	68.2	5.91	23.3	67	0.97	0.75	0.75	0.75	0.74	0.79
12mT-80°C	478	22.4	76.06	6.59	25.7	67	0.98	0.82	0.92	0.83	0.81	0.87
22mT-20°C	541	24	80.4	6.9	27.4	68	0.99	0.88	0.87	0.88	0.87	0.90
22mT-80°C	452	15.9	55.9	5.1	19.1	31	0.45	0.61	0.65	0.61	0.58	0.58
28mT-20°C	540	25.5	84.5	7.32	28.8	68	0.99	0.92	0.92	0.92	0.93	0.94
28mT-80°C	461	23.8	78.33	6.8	26.7	73	1	0.86	0.86	0.86	0.89	0.89

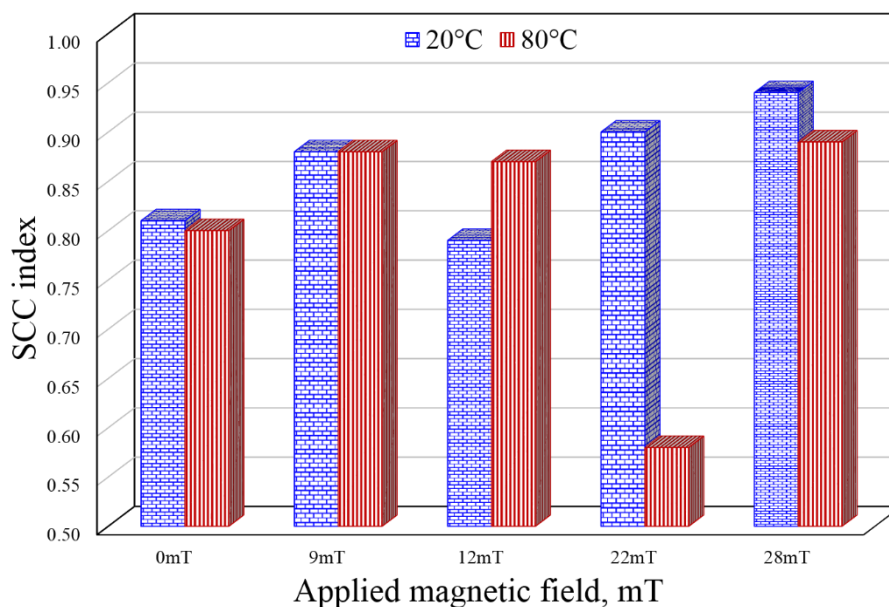


Figure 8. Effect of temperature on SCC index.

The effect of testing temperature on SCC of ASSs in boiling saturated magnesium chloride solution using a constant load method was evaluated by Alyousif and Nishimura [35-37]. The authors used a relationship between the time to failure and a reciprocal of test temperature and the data fell in two straight lines on a semi-logarithmic scale. The authors found that the linearity of the relationship may be used to predict the time to failure for the stainless steels in the corrosive environment.

Nishimura et al. [38] investigated the effect of strain rate and pH change on the susceptibility to SCC in an acidic environment in ASSs. The results obtained from the SSR test were compared with the constant loading method and were discussed in terms of the formation of slip steps, dissolution current and film formation rate. Meanwhile, Takano et al. [39, 40] observed that the strain rate dictates the deterioration process in ASS and found that the corrosion process takes place at high strain rates whilst the SCC process is favored at slow strain rates, occurring preferentially at slip steps .

3.3. Fractography analysis

The fracture characteristics of the AISI type 304 ASS were observed in the SEM. Figures 9 and 10 show secondary electron images of the fracture surfaces after performing the SSR test in air and in the MgCl₂ solution at 20°C and 80°C for the different applied magnetic fields.

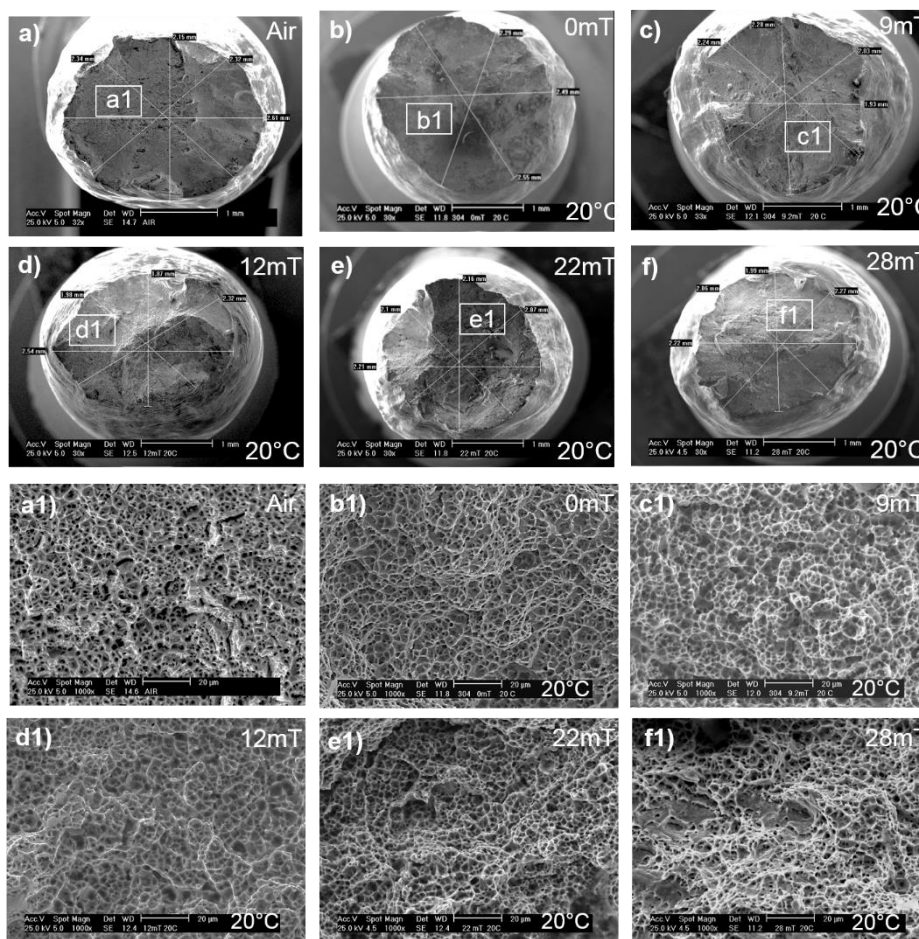


Figure 9. SEM images of the fracture surfaces of samples tested in; a) air and b-f) tested in MgCl₂ solution at 20°C with different magnetic field applied during welding; a1)-f1) SEM images at higher magnification of selected areas.

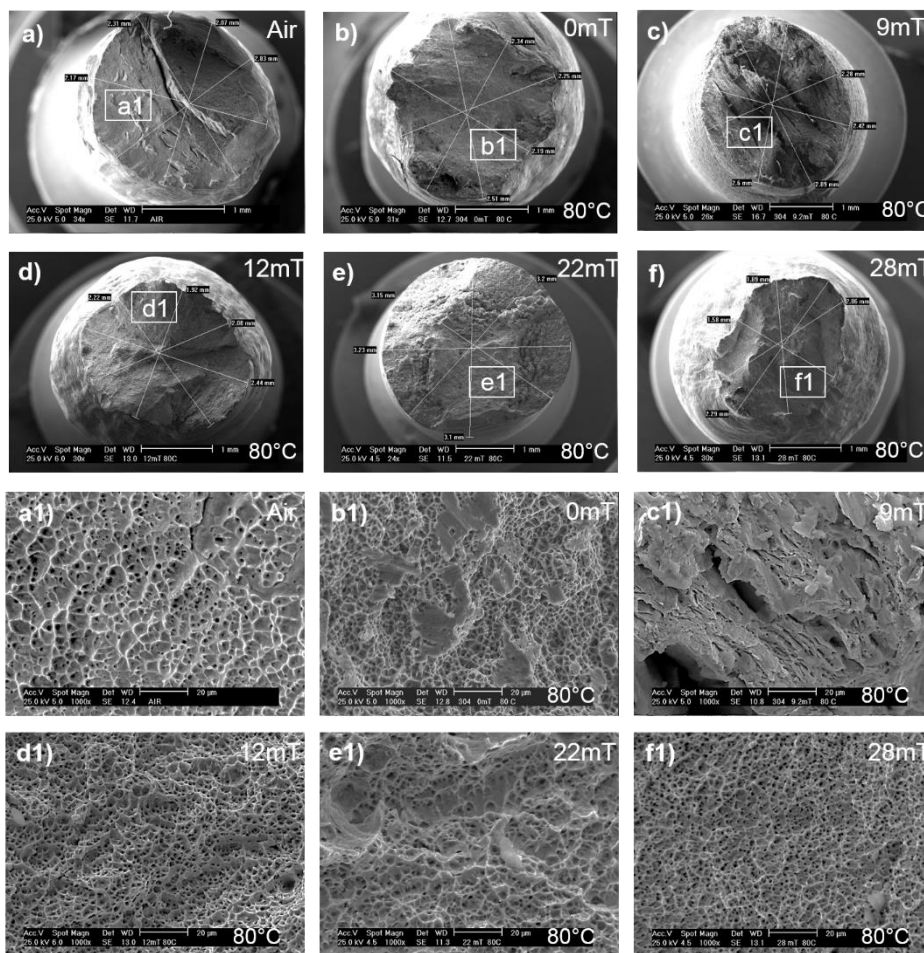


Figure 10. SEM images of the fracture surfaces of samples tested in a) air, and b-f) tested in MgCl₂ solution at 80°C with different magnetic field applied during welding; a1)-f1) SEM images at higher magnification of selected areas.

Figures 9a)-f) and 10a)-f) show top views of the fractured surfaces exhibiting in some cases the neck formation and deformation prior to fracture. Additionally, these images show the measurements of fracture diameter used to calculate the reduction area (*RA*). Figures 9a1)-f1) and 10a1)-f1) show the features of the fractures as observed in the SEM at high magnification. Irrespective of the testing medium and welding condition, the tested specimens presented ductile fracture.

In the fractographies, it is observed the typical coalescence of micro dimples, which grow in the direction of the strain generated during the SRR test. This type of ductile fracture is characteristic in ASSs. The fracture mode for type 304 ASS was predominantly transgranular, this appearance is more evident as the temperature increases. From some selected surface fractures, energy dispersive X-ray (EDX) analyses were performed and the results are shown in Figure 11. It seems that most of the fractures show the presence of chromite (FeCr₂O₄). These particles were also found to contain magnesium, aluminum or titanium (among other elements).

AISI 304 ASS is highly prone to martensitic transformation when it is cold deformed because it has a metastable structure. The transformation of martensite induced by deformation at the grain

boundaries acts as potential sites for hydrogen lodging. It is known that the presence of martensite induces hydrogen embrittlement due to the very high hydrogen diffusivity coefficient and very small hydrogen content as compared to that of austenite [41].

Since cold deformation can induce microstructural transformation, intergranular cracking can be attributed to the diffusion of hydrogen, which in turn induces embrittlement in selective zones as grain boundaries, triple points and second phase boundaries where the hydrogen permeation increases its diffusivity.

Sun et al. [42] found that an intergranular cracking path may be induced through the martensite structure which facilitated higher diffusion rates of hydrogen at high temperatures. It is important to note that increasing the amount of martensite content in the structure produced by applied stress (or strain) will increase the susceptibility of the material to SCC. It was observed that the differences in the fracture appearances for ASS were attributed to a difference in martensite formation at the grain boundaries as described above. The fracture observations were carried out with the objective to ascertain if there were secondary cracks in the gauge section of the SSRT specimens as well as to observe the type of fracture (intergranular or transgranular) and determine the zone of failure of the SSRT specimens.

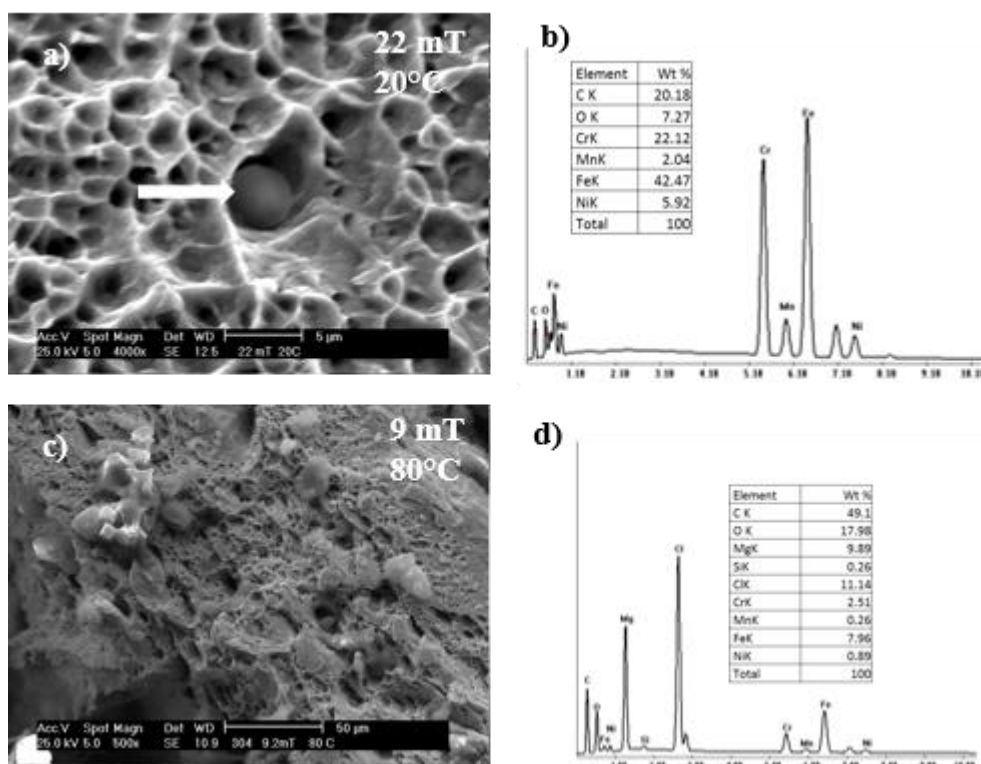


Figure 11. a) SEM images of samples tested in MgCl₂ solution, a) showing the presence of some inclusions and micro-voids, b) EDX obtained from the inclusion, c) showing the corrosion products and d) EDX spectra obtained from the area shown in c).

Macrographs of the longitudinal sections of the SSRT specimens tested in air and the MgCl₂ solution showing the failure zone are presented in Figure 12. All the specimens for the different conditions failed in the weld bead, except for the specimens welded with 9mT. It is well known that

AISI 304 stainless steel is a meta-stable material that experiences microstructural transformation due to plastic deformation, inducing the formation of α' -martensite. Thus, it is highly likely that when deformation occurs, an increment in α' -martensite arises increasing in consequence the hardness in the HAZ. Chen et al. [6] found that α' -martensite increased up to 10 % when deformation was induced. The apparition of this phase has a rather significant drawback on the SCC susceptibility for MgCl_2 at 143°C. The filler metal ER309L yields a weld metal formed by austenite and δ -ferrite as observed in the optical micrographs of Figure 6. Thiago et al. [43] reported that due to the more electrochemical active behavior of ferrite, the fusion zone is prone to fail under SCC in MgCl_2 solution, as a result, the weld metal is the weakest region of the welded joint. Thus, failure of the welded specimens at the weld metal was dictated in principle by the presence of δ -ferrite and further compromised by the precipitation of α' -martensite as a result of the strain induced during the SSRT. Failure of the 9 mT weld at the base metal means that the electromagnetic stirring of the weld pool and the electromagnetic interaction of low intensity in the solid weld metal gave rise to an optimized microstructure in this zone so that the strain induced α' -martensite formation was the predominating mechanism for this welding condition.

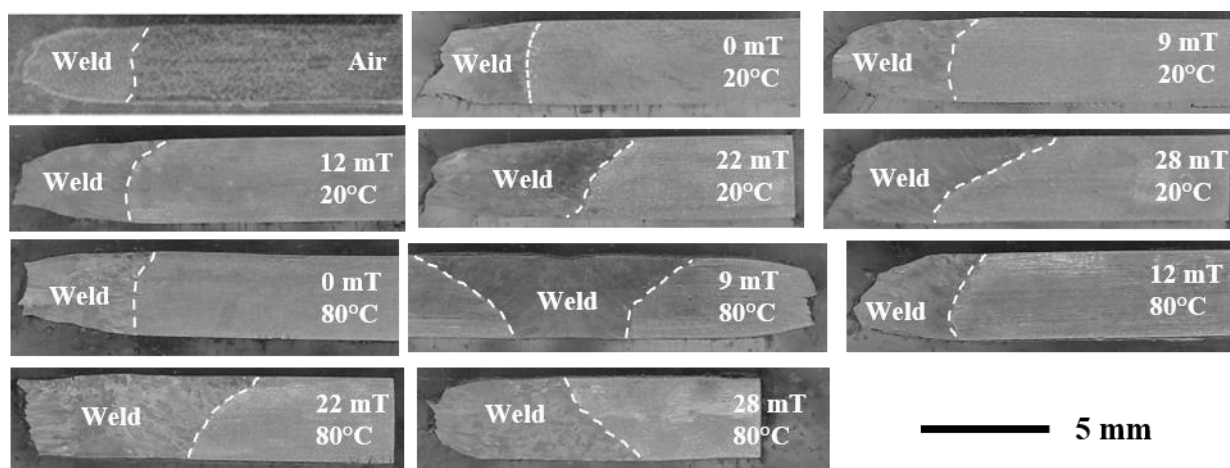


Figure 12. Longitudinal cross-section of samples tested at 20 and 80°C.

Complementary to assess the susceptibility of the welds to SCC through *RAR*, *PER*, *TFR*, *ELR*, and ϵR , the samples were observed in the SEM at low magnifications in order to observe if there were secondary cracks in the gauge section of the broken samples, if so, it would be indicative of SCC. Figure 13 shows the longitudinal cross-section of samples tested at 20 and 80°C for the different welding conditions. SEM examination focused on samples with I_{sc} lower than 0.8. Apparently, not secondary cracks were observed at lower magnifications, except for the 22mT weld tested at 80°C.

The longitudinal cross-section of the samples was observed at higher magnifications. Figure 14 exhibits representative SEM images obtained for the different welds at 20 and 80°C showing details of some pits and cracks in the gauge section of the SSRT specimens. When SSRT samples of base metal were tested in MgCl_2 at 20 and 80°C some cracks and pits were observed. Analysis of several images revealed that some of these pits evolve into cracks. These cracks initiated at the bottom of the pits. The

top image in the mid, clearly reveals the preferential attack in the ferrite bands of the as-received AISI 304 ASS.

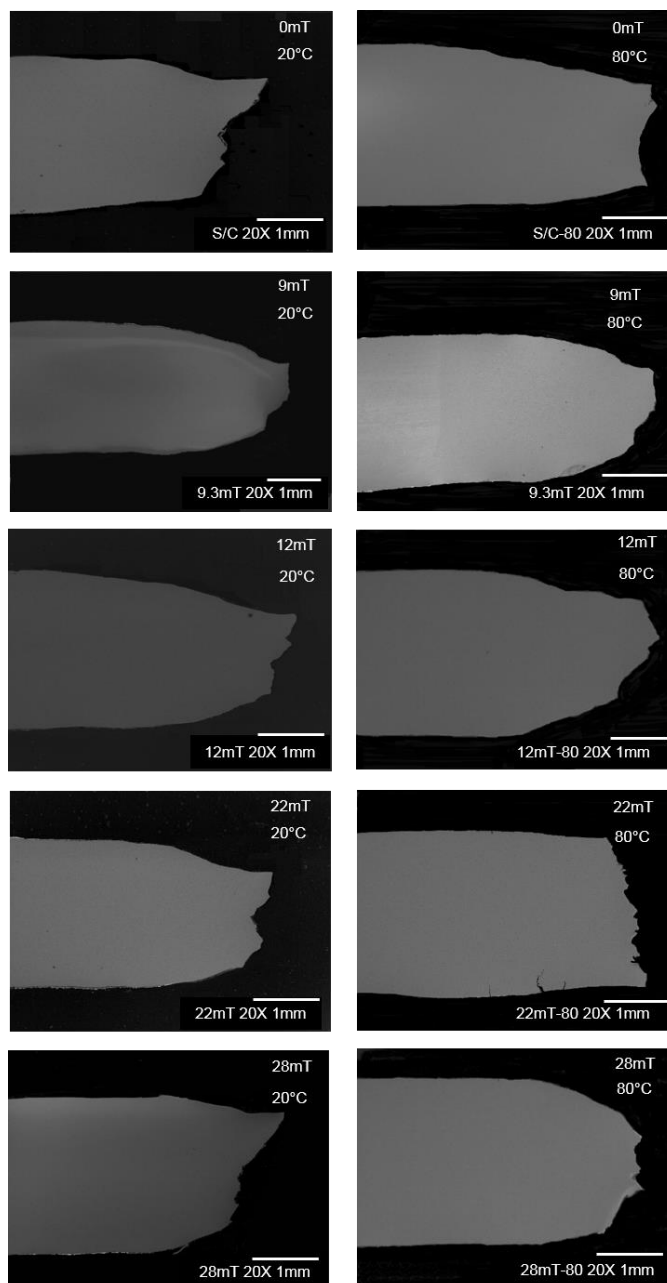


Figure 13. Longitudinal cross-section of samples tested at 20 and 80°C.

The results of SCC index (I_{sc}) presenting values lower than 0.8 (0mT-80°C; 12mT-20°C; 22mT-80°C) showed good correlation with the experimental evidence obtained in the SEM. These findings indicate that the most susceptible samples to SCC are the 22mT welded joints tested at 80°C. According to the SEM images shown in Figure 13 and 14, it is clear that these samples showed some cracks in the gauge section. As expected, the $MgCl_2$ solution has high content of chlorine reducing the pH of the solution and that increases the activity coefficient of the hydrogen ions [44].

The electrochemical reactions that take place at the surface of the nucleated cracks conduct to oxygen depletion in the cathodic reaction, $O_2 + 2H_2O + 4e^- \leftrightarrow 4OH^-$. This reduction in oxygen occurs at the whole surface of the crack. Nonetheless, the kinetics of cathodic reactions once a crack is growing, deplete the oxygen faster within the crack as the surface area is greater. Thus, as the oxygen is depleted, a more negative corrosion potential is produced at the crack tip and the anodic dissolution of major elements materializes in a separate electrochemical cell as follows: $M \rightarrow M^{n+} + e^-$, $H_2O + e^- \rightarrow H + OH^-$ and/or $H^+ + e^- \rightarrow H$. This effect leads to the increment of Cr^{3+} , Fe^{2+} and Ni^{2+} ions at the crack tip promoting the hydrolysis in the reaction, that is; $M^{n+} + H_2O \leftrightarrow MOH^{(n-1)+} + H^+$. Thus, the media in the crack tip becomes acidic until pH values achieve a more stable value as equilibrium between metal ions and H^+ is approaching [45]. Additionally, the chloride ions promote the incubation of pitting, and due to tensile stresses, cracks are susceptible to nucleate and grow in the weld metal [46].

The welded joints of the AISI 304 ASS that exhibited the best resistance to environmental cracking and pitting were specimens welded with the simultaneous application of 9 and 28 mT. This might be attributed to the microstructure obtained in the weld metal, where the electromagnetic interaction of low intensity between the welding current and the electric current of the coil gives rise to electromagnetic stirring of the weld pool and induce grain refinement during its solidification. In addition, the decrease of residual stress in welds made under electromagnetic fields can be attributed to alteration of the microstructure in weld metal. According to Chen et al. [47], this effect can extend to the HAZ and the lattice of crystal structures of γ and δ phases can be shrunk during transformation for the different compactness and the extra volume released from the transformation contributes to decreasing residual stresses. Thus, the reduction of residual stresses in the welded joints aids to improve their behavior to SCC [48].

4. CONCLUSIONS

From the study conducted on the susceptibility to SCC of AISI 304 stainless steel base metal and welded joints obtained under the application of different magnetic fields exposed to 20%-MgCl₂ solution through SSR testing, the following conclusions are derived:

1) The application of axial magnetic fields of low intensity during GMAW of cold deformed AISI 304 stainless steel increased its resistance to pitting and intergranular corrosion. This behavior is associated to the interaction between the external magnetic field applied during welding and the magnetic field induced by the welding current, which promoted Cr redistribution in the austenitic matrix improving the resistance to SCC.

2) The SCC assessment was carried out in function of the results of *RAR*, *PER*, *TFR*, *ELR*, and ϵR . According to the results the samples tested in the 20%-MgCl₂ solution at room temperature and 80°C exhibited low susceptibility to SCC. SEM observations revealed secondary cracks, most of them originated by pits, which were observed mainly for samples of the as-received base material and welded joints with 22mT at 80°C. The SCC susceptibility increased with temperature. It was observed that the mechanical properties decreased slightly with temperature.

3) SEM observations showed that most of SSRT samples tested in MgCl₂ solution failed in the weld bead, exhibiting a ductile fracture. Most of the fracture surfaces showed intergranular cracking. The failure mechanism for AISI 304 ASS is dictated by the formation of α' -martensite at the grain boundaries in the HAZ and in the weld metal because of the presence of δ -ferrite, which promotes the precipitation of martensite during SSR testing.

4) The welds of AISI 304 stainless steel that exhibited better resistance to environmental cracking and pitting were those obtained applying 9 and 28 mT during welding. The fact that the latter weld showed penetration problems as a result of the magnetic field applied, means that the best welded joint for SCC was obtained by welding with 9 mT. For this weld, irrespective of testing temperature, the *I*_{SSC} values were quite even and failure occurred in the base metal. This is attributed to the grain refined microstructure induced in the weld metal by electromagnetic stirring.

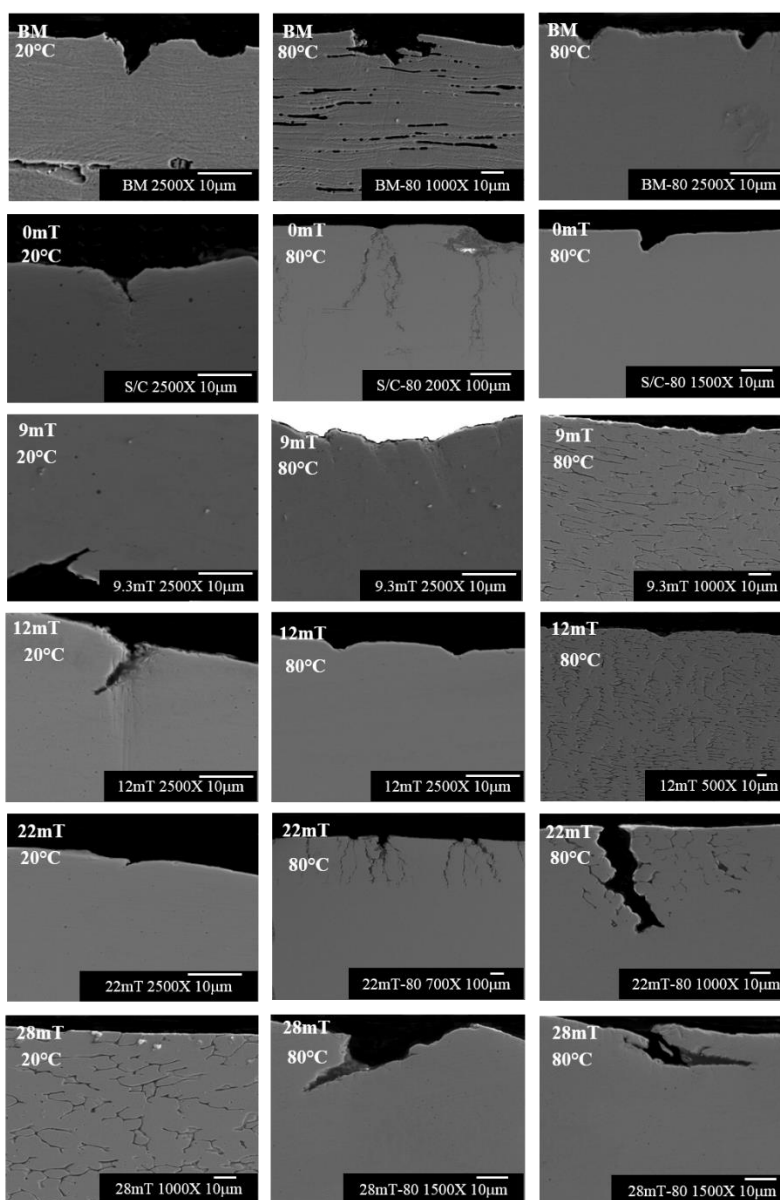


Figure 14. SEM images of the longitudinal cross-section for specimens of the as-received AISI welded with different magnetic fields and SSR tested at 20 and 80°C.

ACKNOWLEDGEMENTS

The authors thank the National Council of Science and Technology (CONACyT) and Mexican Petroleum Institute IMP for supporting this project.

References

1. A.Abou-Elazm, R. Abdel-Karim, I. Elmahallawi and R. Rashad, *Corros. Sci.*, 51 (2009), 203.
2. I. Bösing, I. Bobrov, J. Epp, M. Baune and J. Thöming, *Int. J. Electrochem. Sci*, 15 (2020), 319.
3. H. Tukur and L. Yonghao, *Int. J. Electrochem. Sci*, 15 (2020), 2115.
4. J. Cabral-Miramontes, C. Gaona-Tiburcio and F. Almeraya-Calderón, *Int. J. Electrochem. Sci*, 12 (2017), 4928.
5. N. Parnian, *Mater. Des. (1980-2015)*, 36 (2012), 788.
6. H. Chen, X.Z. Guo, W.Y. Chu, K.W. Gao, Y.B. Wang, Y.J. Su and L.J. Qiao, *Mater. Sci. Eng.: A*, 358 (2003), 122.
7. S.C. Bali, V. Kain and V.S. Raja, *Corros.*, 65 (2009), 726.
8. R.H. Jones, Stress-corrosion cracking, ASM International, (1992).
9. M. Kowaka and T. Kudo, *Trans. Jpn. Inst. Met.*, 16 (1975), 385.
10. A. G36, Standard practice for evaluating stress-corrosion-cracking resistance of metals and alloys in boiling magnesium chloride solution, in: 03.02, USA, 1994.
11. P. De Tiedra and Ó. Martín, *Mater. Des.*, 49 (2013), 103.
12. C. Garcia, M.P. de Tiedra, Y. Blanco, O. Martin and F. Martin, *Corros. Sci.*, 50 (2008), 2390.
13. R. Singh, G. Das, P.K. Singh and I. Chattoraj, *Metall. Mater. Trans. A*, 40 (2009), 1219.
14. M. Milad, N. Zreiba, F. Elhalouani and C. Baradai, *J. Mater. Process. Technol.*, 203 (2008), 80.
15. P. De Tiedra, Ó. Martín, C. García, F. Martín and M. López, *Corros. Sci.*, 54 (2012), 153.
16. F.F. Curiel, R. García, V.H. López and J. González-Sánchez, *Corros. Sci.*, 53 (2011), 2393.
17. F.F. Curiel, R. García, V.H. López and J. Gonzalez-Sanchez, *Mater. Trans.*, 52 (2011), 1701.
18. I.S. Cortés-Cervantes, V.H. López-Morelos, Y. Miyashita, R. García-Hernández, A. Ruiz-Marines and M.A. Garcia-Renteria, *Inter. J. Adv. Manuf. Technol.*, 99 (2018), 2849.
19. M.A. García-Rentería, V.H. López-Morelos, R. García-Hernández, L. Dzib-Pérez, E.M. García-Ochoa and J. González-Sánchez, *Appl. Surf. Sci.*, 321 (2014), 252.
20. M.A. García Rentería, V.H. López Morelos, R. García Hernández, F.F. Curiel López and J. Lemus-Ruíz, *Mater. Sci. Forum*, 755 (2013), 61.
21. R.C. Rafael García, Diana L. García, and Víctor H. López, Effect of the Perpendicular Electromagnetic Field in the 304 Austenitic Stainless Steel Welding in a Single Pass, in: R. Pérez Campos, Contreras Cuevas, Antonio, Esparza Muñoz, Rodrigo (Ed.) Materials Characterization, Springer, Switzerland, 2015, pp. 119.
22. F.F. Curiel, R. García, V.H. López, M.A. García and J. Lemus, *Mater. Trans.*, 54 (2013), 122.
23. M. Malinowski, G. Den and W.J.P. Vink, *Welding J.*, 02 (1990), 52s.
24. J.C. Villafuerte and H.W. Kerr, *Welding Journal*, 01 (1990),
25. S. Nakamichi, S. Tsurekawa, Y. Morizono, T. Watanabe, M. Nishida and A. Chiba, *J. Mater. Sci.*, 40 (2005), 3191.
26. D. San Martín, K.W.P. Aarts, P.E.J. Rivera-Díaz-del-Castillo, N.H. van Dijk, E. Brück and S. van der Zwaag, *J. Magn. Magn. Mater.*, 320 (2008), 1722.
27. NACE-TM198, Slow strain rate test method for screening corrosion-resistance alloys (CRAs) for stress corrosion cracking in sour oilfield service, in, National Association of Corrosion Engineers, 2004.
28. G.M. Ugiansky, Stress Corrosion Cracking-the Slow Strain Rate Technique, American Society for Testing and Materials, (1979).
29. ASTM-G129, Slow Strain Rate Testing to Evaluate the Susceptibility of Metallic Materials to Environmentally Assisted Cracking, in, ASTM, 2006.

30. B.Y. Fang, R.L. Eadie, W.X. Chen and M. Elboujdaini, *Corros. Eng. Sci. Technol.*, 45 (2010), 302.
31. G. Van Boven, W. Chen and R. Rogge, *Acta Mater.*, 55 (2007), 29.
32. T. Shoji, Z. Lu and H. Murakami, *Corros. Sci.*, 52 (2010), 769.
33. Z. Zhengwu, M. Xiuquan, W. Chunming and M. Gaoyang, *Mater. Character.*, 164 (2020), 110311.
34. R. Chen, P. Jiang, X. Shao, G. Mi and C. Wang, *J. Mater. Process. Technol.*, 254 (2018), 114.
35. O.M. Alyousif and R. Nishimura, *Corros. Sci.*, 48 (2006), 4283.
36. R. Nishimura, *Corros. Sci.*, 49 (2007), 81.
37. O.M. Alyousif and R. Nishimura, *Corros. Sci.*, 49 (2007), 3040.
38. R. Nishimura and Y. Maeda, *Corros. Sci.*, 46 (2004), 769.
39. M. Takano, *Corros.*, 30 (1974), 441.
40. M. Takano and N. Totsuka, *Corros.*, 36 (1980), 36.
41. O.M. Alyousif and R. Nishimura, *Inter. J. Corros.*, 2012 (2012),
42. X. Sun, J. Xu and Y. Li, *Acta Metall.*, 37 (1989), 2171.
43. T. AmaroVicente, L.A. Oliveira, E.O. Correa, R.P. Barbosa, V.B.P. Macanhan and N.G.d. Alcântara, *Met.*, 8 (2018), 195.
44. J. Mankowski and Z. Szklarska-Smialowska, *Corros. Sci.*, 15 (1975), 493.
45. L.G. Bland and J.S. Locke, *npj Mater. Degrad.*, 1 (2017), 12.
46. U. Martin, J. Ress, J. Bosch and D.M. Bastidas, *Electrochim. Acta*, 335 (2020), 135565.
47. R. Chen, P. Jiang, X. Shao, G. Mi and C. Wang, *Inter. J. Adv. Manuf. Technol.*, 91 (2017), 3437.
48. M. Mochizuki, *Nucl. Eng. Des.*, 237 (2007), 107

© 2021 The Authors. Published by ESG (www.electrochemsci.org). This article is an open access article distributed under the terms and conditions of the Creative Commons Attribution license (<http://creativecommons.org/licenses/by/4.0/>).